Simulation of the Beating Heart Based on Physically Modeling a Deformable Balloon

Damien Rohmer, Arkadiusz Sitek, Grant T Gullberg

▶ **To cite this version:**

Damien Rohmer, Arkadiusz Sitek, Grant T Gullberg. Simulation of the Beating Heart Based on Physically Modeling a Deformable Balloon. Lawrence Berkeley National Laboratory, California, USA. 2006. ⟨hal-03929238⟩

HAL Id: hal-03929238

https://hal.science/hal-03929238v1

Submitted on 8 Jan 2023

HAL is a multi-disciplinary open access archive for the deposit and dissemination of scientific research documents, whether they are published or not. The documents may come from teaching and research institutions in France or abroad, or from public or private research centers.

L'archive ouverte pluridisciplinaire **HAL**, est destinée au dépôt et à la diffusion de documents scientifiques de niveau recherche, publiés ou non, émanant des établissements d'enseignement et de recherche français ou étrangers, des laboratoires publics ou privés.

HAL Authorization

Simulation of the Beating Heart Based on Physically Modeling a Deformable Balloon

Damien Rohmer, Arkadiusz Sitek, Grant T. Gullberg
The authors are with the Division of Life Science, E.O. Lawrence Berkeley National Laboratory,
1 Cyclotron Road, Berkeley, CA 94720, USA.

July 18, 2006

Abstract

The motion of the beating heart is complex and creates artifacts in SPECT and x-ray CT images. Phantoms such as the Jaszczak Dynamic Cardiac Phantom are used to simulate cardiac motion for evaluation of acquisition and data processing protocols used for cardiac imaging. Two concentric elastic membranes filled with water are connected to tubing and pump apparatus for creating fluid flow in and out of the inner volume to simulate motion of the heart. In the present report, the movement of two concentric balloons is solved numerically in order to create a computer simulation of the motion of the moving membranes in the Jaszczak Dynamic Cardiac Phantom. A system of differential equations, based on the physical properties, determine the motion. Two methods are tested for solving the system of differential equations. The results of both methods are similar providing a final shape that does not converge to a trivial circular profile. Finally, a tomographic imaging simulation is performed by acquiring static projections of the moving shape and reconstructing the result to observe motion artifacts. Two cases are taken into account: in one case each projection angle is sampled for a short time interval and the other case is sampled for a longer time interval. The longer sampling acquisition shows a clear improvement in decreasing the tomographic streaking artifacts.

keywords: Differential Equation, Numerical Method, Physically Based Modeling, Tomography Artifacts

1 Introduction

WHEN imaging the heart, the movement of it creates artifacts which are hard to model due to the complexity of its motion. One can use both physical and computer generated phantoms to simulate the cardiac motion in the evaluation of imaging and data processing protocols. One physical phantom is the Jaszczak Dynamic Cardiac Phantom.

The Jaszczak Dynamic Cardiac Phantom is used to evaluate imaging techniques applied to emission tomography such as SPECT. The phantom consists of the standard Jaszczak cardiac torso phantom with two concentric inflatable balloon inserts and pump apparatus (see Fig. 1). A pump inflates the balloons with fluid pumped through tubing into and out of the inner balloon insert, which is sealed and attached to the tubing. With proper adjustments of pressures both externally and internally the balloons will inflate and deflate simulating the motion of the heart. A radioisotope can be injected into the spacing between the two balloons to simulate uptake of isotope in myocardium tissue or within the inter volume to simulate activity in the blood of the left ventricular cavity. The phantom with the simulated beating heart is used to simulate an imaging experiment of a human beating heart. The phantom simulates the motion of the boundaries of the heart but does not simulate the twisting and true deformation of the heart wall [1–3].

Here we solve for the motion of the two balloon inserts by solving numerically a system of differential equations that represents the physics for the equilibrium of forces. The numerical solution can then be used to compare with results that are obtained in applying our mechanical models [4–7] to imaging data of the Jaszczak Dynamic Cardiac Phantom. Our simulation uses two plastic ballons for a simple model of the ventricle (Fig. 2) which can be dilated and contracted to simulate the motion. The inner balloon models the endocardium and the outer balloon corresponds to the epicardium. The space between the two balloons simulates the heat wall. Our purpose is to numerically simulate the motion of these balloon

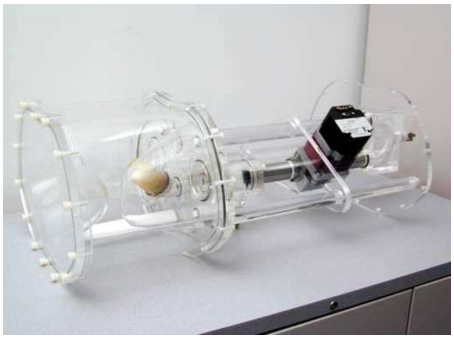

Fig. 1: Picture of the Jaszczak Dynamic Cardiac Phantom used to evaluate the motion of the heart with two concentric balloons in the middle of the torso.

inserts in order to create a numerical model of the motion of the Jaszczak Dynamic Cardiac Phantom.

The balloon has an initial cylindrical shape of length h with a spherical apex of radius R (R_0 for the interior and R_1 for the exterior semi-circle) see Table 1 and Fig. 2.

Table 1: Dimensions of the balloons

	h (cm)	R (cm)
interior	8.5	1.75
exterior	8.5	2.75

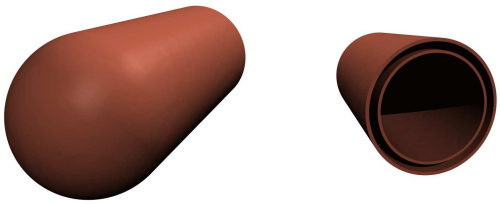

(a) 3D model of the exterior balloon

(b) View of the flat end of the two concentric balloons

Fig. 2: Initial cylindrical shape of the balloons with spherical apex

The problem can be treated directly in a $2D$ plane containing the axis of revolution (see Fig. 3) since the material is assumed to be completely isotropic around its circumferential direction. Afterwards, the results are applied in $3D$ by revolution.

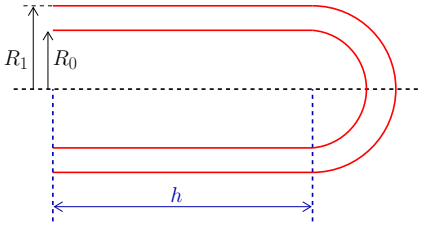

Fig. 3: Slice of the balloons for the $2D$ numerical study.

Table 2: Formulas for the balloon characteristics

volume	$\pi R^2\left(h+\frac{4}{6}R\right)$
surface delimited by the $2D$ curve	$\pi R\left(2h+\frac{R}{2}\right)$
length of the $2D$ curve	$2h+\pi R$

Some formulas for the volume of the balloon, the area filled by the boundaries in the $2D$ plane and the length of these boundaries in $2D$ are summarized in Table 2.

2 Model of the Physical Forces

The balloon is subject to forces which determine how the balloon deforms. In this report we use a model of forces that has been used to simulate deformable material made of cloth. The description of this problem and its solution were first introduced by D. Terzopoulos *et al.* in 1987 [8].

2.1 Pressure Action

Let the vector $\mathbf{c}$ define the parametric $2D$ curve of the balloon parameterized by the parameter s, such that $\mathbf{c}(s) = \Big(c_x(s), c_y(s)\Big)$, where x defines the direction along the axis of rotation and y is the perpendicular direction.

The shape is subject to the internal pressure that the water applies to the inner membrane. Considering only the static behavior of the water, fluid mechanics indicates that the action of the water on the balloon is constantly normal to its curve. Moreover, neglecting the effect of gravity, the magnitude of the force due to pressure is constant along the membrane.

In $2D$, each small arc of length $\mathrm{d}L$ is subject to a constant force of intensity f. If $\mathbf{n}(s)$ defines the normalized exterior normal of the curve at each position $\mathbf{c}(t)$, the pressure force $\mathbf{F}_p$ can be expressed by

$$\mathbf{F}_p(s) = f\,\mathbf{n}(s)\ . \tag{1}$$

The normal can be defined by the curve itself. The tangent vector $\boldsymbol{\tau}$ is given by the derivative of the parametric curve $\mathbf{c}$ with respect to s [9]. Then any normal vector $\mathbf{n}'$ ($\mathbf{n}$ is normalized where $\mathbf{n}'$ is not necessarily) can be defined by $\boldsymbol{\tau} \cdot \mathbf{n}' = 0$. Therefore, an external normal can be defined by:

$$\mathbf{n}'(s) = \begin{pmatrix} -c'_y(s) \\ c'_x(s) \end{pmatrix} . \tag{2}$$

Equation 1 can then be rewritten by normalizing $\mathbf{n}'$:

$$\mathbf{F}_p(s) = f \frac{\begin{pmatrix} -c'_y(s) \\ c'_x(s) \end{pmatrix}}{\sqrt{{c'_x}^2(s) + {c'_y}^2(s)}} , \tag{3}$$

where f is a local constant[1] force parameter.

The force f can be expressed in reference to a global action of the pump exerted on the water. Let us suppose the pump exerts a force F^α on the whole interior surface in order to make the balloon have a percent gain in volume α compared to its resting state. This force is then homogeneous at every position. So for every position defined by $\mathbf{c}(s)$ the action has a magnitude of $\frac{\mathbf{F}^\alpha}{S}$, where S is the total surface area of the shape. Locally, the area element of the membrane (which is a surface of revolution) is $\mathrm{d}S = 2\pi\, c_y \sqrt{{c'_x}^2 + {c'_y}^2}\, \mathrm{d}s$. Then the local force f can be linked to the global force F^α and Eq. 3 can be expressed by:

$$\begin{aligned} \mathbf{F}_p(s) = \quad & \frac{F^\alpha}{2\pi} \frac{1}{\displaystyle\int_c c_y(u) \sqrt{{c'_x}^2(u) + {c'_y}^2(u)}\, \mathrm{d}u} \\ & \times \frac{\begin{pmatrix} -c'_y(s) \\ c'_x(s) \end{pmatrix}}{\sqrt{{c'_x}^2(s) + {c'_y}^2(s)}} , \end{aligned} \tag{4}$$

where F^α is a global parameter independent of the shape itself.

2.2 Membrane Reaction

The membrane of the balloon is elastic and reacts itself with elastic deformations. A comprehensible model of this membrane is to consider it composed of an infinite number of positions all linked with their neighbors by springs. Such a method has been used for instance for $3D$ modeling of muscle in [10].

Each position has two neighbors and two elastic forces act upon them. Let us call $\Delta\mathbf{c}$ the displacement between the current position and the initial shape $\mathbf{c}^0$. The reaction $\mathbf{F}_e$ of the membrane to the exterior forces is then expressed by

$$\begin{aligned} \mathbf{F}_e(s) = \quad & \lambda \left(s + \frac{\mathrm{d}s}{2} \right) \Big(\Delta\mathbf{c}\,(s + \mathrm{d}s) - \Delta\mathbf{c}\,(s) \Big) \\ & + \lambda \left(s + \frac{\mathrm{d}s}{2} \right) \Big(\Delta\mathbf{c}\,(s - \mathrm{d}s) - \Delta\mathbf{c}\,(s) \Big), \end{aligned} \tag{5}$$

where λ is the stiffness of the membrane at each position.

The basic decomposition of the derivative of the product can be recognized and the internal elastic force is

$$\mathbf{F}_e(s) = \Big(\lambda \left(\mathbf{c} - \mathbf{c}^0 \right)' \Big)'(s). \tag{6}$$

It can be noticed that if the stiffness is constant along the curve, this force reduces to the second derivative:

$$\mathbf{F}_e(s) = \lambda \left(\mathbf{c} - \mathbf{c} \right)''(s). \tag{7}$$

2.3 Damping Force

An arbitrary damping force can be added to the model. Since the forces of pressure and elasticity conserve energy, a simulation of a dynamic system would oscillate constantly. To facilitate reaching an equilibrium position, and to model the physical decrease of energy, a fluid friction force is added. This force $\mathbf{F}_d$ is directly proportional to the speed of the variation of the curve $\mathbf{v}_c$:

$$\mathbf{F}_d = -\mu\, \mathbf{v} , \tag{8}$$

where $\mu \in [0, 1]$.

2.4 Boundary Conditions

The forces just described are acting at each position along the curve $\mathbf{c}$. However, the physical model is fixed at the base. Supposing that these contact positions have zero length, the sum of the forces acting on the first and final position of the balloon are zero. If the curve $\mathbf{c}$ is parameterized by s with $s \in [0, 1]$, the boundary conditions are set-up with $\mathbf{F}_p(b) = \mathbf{F}_e(b) = \mathbf{F}_d(b) = \mathbf{0}$ for $b = \{0, 1\}$.

3 Solution

For a given F^α the goal of the simulation is to solve for the curve $\mathbf{c}$ that satifies the equilibrium equation, which is the sum of Eq. 4, 6 and 8 equal to zero:

$$\mathbf{F}_p + \mathbf{F}_e + \mathbf{F}_d = \mathbf{0} . \tag{9}$$

[1] for a fixed curve, actually f depends on $\mathbf{c}$

3.1 Direct Method

3.1.1 Set-up of the equation

A method to solve the problem is to try directly to solve the constraint in Eq. 9 for the final resting state. To solve Eq. 9 the damping force is not needed as the curve goes in one step from the initial to the final static state. Therefore, the damping term is equal to zero. Moreover, the local coefficient f of the pressure force in Eq. 1 can be used as a constant as the curve does not evolve dynamically during the process. Thus, Eq. 3 can be used instead of Eq. 4. The equilibrium condition then gives a system of second order non-linear differential equations $\mathbf{F}(\mathbf{c}, \mathbf{c}', \mathbf{c}'') = \mathbf{0}$:

$$\begin{cases} -\ f\dfrac{c_y'(s)}{\sqrt{{c_x'}^2(s)+{c_y'}^2(s)}} + \left(\lambda\ \left(c_x - c_x^0\right)'\right)'(s) = 0 \\ \\ \quad f\dfrac{c_x'(s)}{\sqrt{{c_x'}^2(s)+{c_y'}^2(s)}} + \left(\lambda\ \left(c_y - c_y^0\right)'\right)'(s) = 0 \end{cases} \tag{10}$$

The system $\mathbf{F}(\mathbf{c}, \mathbf{c}', \mathbf{c}'') = \mathbf{0}$ is a boundary value problem (BVP) with initial and final positions known. In order to solve this system, a finite difference approach is used. This system of equations can be rewritten in a more elegant formulation using complex variable notation: $z(s) = c_x(s) + i\, c_y(s)$. In the case of a constant stiffness λ along the shape of the curve, the system of equations is:

$$z'' + i\,\frac{f}{\lambda}\,\frac{z'}{|z'|} = z^{0\prime\prime}\ . \tag{11}$$

It is shown in the appendix that the forcing term z^0 is responsible for the global non linearity of the system of equations.

3.1.2 Discretization

To solve the system of differential equations in Eq. 10, the system is defined numerically at a set of N positions separated in material coordinates by Δs. Since a discrete form of the elastic force is known by the problem, it is then probably better to keep this discretization. The pressure is discretized by a classical central second order method. The damping term doesn't need to be discretized to this level as it is equal to zero. Each term of the equation $\mathbf{F}_p + \mathbf{F}_e$ is then discretized. The elastic force is separated into $\mathbf{F}_{e_1}$ and $\mathbf{F}_{e_2}$ as seen in Fig 4. This process gives a system of non-linear equations of dimension $N-2$ with the first and the last positions fixed. The equation $\mathbf{F}_p + \mathbf{F}_{e_1} + \mathbf{F}_{e_2} = 0$ can be expressed by:

$$\begin{aligned} &-f\frac{c_y(n+1)-c_y(n-1)}{\sqrt{\Big(c_y(n+1)-c_y(n-1)\Big)^2+\Big(c_x(n+1)-c_x(n-1)\Big)^2}} \\ &+\lambda\left(n+\tfrac{1}{2}\right)\frac{\Big(\Big(c_x(n+1)-c_x(n)\Big)-\Big(c_x^0(n+1)-c_x^0(n)\Big)\Big)}{\Delta t} \\ &+\lambda\left(n-\tfrac{1}{2}\right)\frac{\Big(\Big(c_x(n-1)-c_x(n)\Big)-\Big(c_x^0(n-1)-c_x^0(n)\Big)\Big)}{\Delta t} \\ &= 0 \end{aligned}$$

$$\begin{aligned} &f\frac{c_x(n+1)-c_x(n-1)}{\sqrt{\Big(c_y(n+1)-c_y(n-1)\Big)^2+\Big(c_x(n+1)-c_x(n-1)\Big)^2}} \\ &+\lambda\left(n+\tfrac{1}{2}\right)\frac{\Big(\Big(c_y(n+1)-c_y(n)\Big)-\Big(c_y^0(n+1)-c_y^0(n)\Big)\Big)}{\Delta t} \\ &+\lambda\left(n-\tfrac{1}{2}\right)\frac{\Big(\Big(c_y(n-1)-c_y(n)\Big)-\Big(c_y^0(n-1)-c_y^0(n)\Big)\Big)}{\Delta t} \\ &= 0 \end{aligned}$$

The two considered forces in the discrete case are shown in Fig. 4

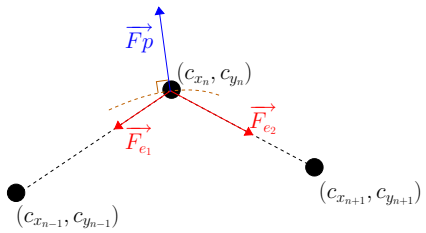

Fig. 4: Force due to pressure (in blue) and forces due to elasticity (in red) on a discrete position (middle black dot). Each position has two neighbors in which the forces of elasticity are directed.

3.1.3 Method of solution

The system of equations can be seen as a large vectorial function $\mathbf{F}$ of $2N$ variables $(c_{x_1}, c_{y_1}, c_{x_2}, \ldots, c_{x_N}, c_{y_N})$. The solution satisfies:

$$\begin{aligned} &\mathbf{F}\Big((c_{x_i}, c_{y_i})_{i\in[\![2,N-1]\!]}\Big) = 0_{\mathbb{R}^2} \\ \Leftrightarrow &\begin{cases} \mathbf{F}^x\Big((c_{x_i}, c_{y_i})_{i\in[\![2,N-1]\!]}\Big) = 0 \\ \mathbf{F}^y\Big((c_{x_i}, c_{y_i})_{i\in[\![2,N-1]\!]}\Big) = 0 \end{cases} \end{aligned} \tag{12}$$

In order to solve this equation, Newton's iterations are used. Let us call $\mathbf{Z}$ the vector such that $\mathbf{Z}_{2n+1} = c_{x_n}$ and $\mathbf{Z}_{2n} = c_{y_n}$. A starting position is chosen with $\mathbf{Z}^0 = (c_x^0, c_y^0)$, and the following iteration is performed until convergence:

$$\mathbf{Z}^{n+1} = \mathbf{Z}^n - \mathrm{DF}^{-1}\left(\mathbf{Z}^n\right) \cdot \mathbf{F}\left(\mathbf{Z}^n\right) \ , \qquad (13)$$

where DF is the Jacobian matrix defined by

$$\mathrm{DF}_{ij}\left(\mathbf{Z}^n\right) = \frac{\partial \mathbf{F}_i}{\partial \mathbf{Z}_j^n}\left(\mathbf{Z}^n\right) \ .$$

The Newton method is supposed to converge quadratically if the solution is close enough to a root of the function $\mathbf{F} : (\mathbf{c}, \mathbf{c}', \mathbf{c}'') \mapsto \mathbf{F}(\mathbf{c}, \mathbf{c}', \mathbf{c}'')$. However, the initial position can be far from the final state and the convergence can be slow as the function is not quadratic.

In order to obtain a precise iteration, the Jacobian is calculated exactly for the discrete problem:

$$\left\{\begin{array}{l}
\frac{\partial \mathbf{F}_n^x}{\partial c_{x_n}} = \frac{\partial \mathbf{F}_n^y}{\partial c_{y_n}} = -\frac{1}{\Delta t}\left(\lambda_{n+\frac{1}{2}} + \lambda_{n-\frac{1}{2}}\right) \\
\frac{\partial \mathbf{F}_n^x}{\partial c_{y_n}} = \frac{\partial \mathbf{F}_n^y}{\partial c_{x_n}} = 0 \\
\frac{\partial \mathbf{F}_n^x}{\partial c_{x_{n-1}}} = -f\,\frac{\left(c_{x_{n+1}} - c_{x_{n-1}}\right)\left(c_{y_{n+1}} - c_{y_{n-1}}\right)}{n_n^3} + \frac{\lambda_{n-\frac{1}{2}}}{\Delta t} \\
\frac{\partial \mathbf{F}_n^x}{\partial c_{x_{n+1}}} = +f\,\frac{\left(c_{x_{n+1}} - c_{x_{n-1}}\right)\left(c_{y_{n+1}} - c_{y_{n-1}}\right)}{n_n^3} + \frac{\lambda_{n+\frac{1}{2}}}{\Delta t} \\
\frac{\partial \mathbf{F}_n^y}{\partial c_{y_{n-1}}} = +f\,\frac{\left(c_{x_{n+1}} - c_{x_{n-1}}\right)\left(c_{y_{n+1}} - c_{y_{n-1}}\right)}{n_n^3} + \frac{\lambda_{n-\frac{1}{2}}}{\Delta t} \\
\frac{\partial \mathbf{F}_n^y}{\partial c_{y_{n+1}}} = -f\,\frac{\left(c_{x_{n+1}} - c_{x_{n-1}}\right)\left(c_{y_{n+1}} - c_{y_{n-1}}\right)}{n_n^3} + \frac{\lambda_{n+\frac{1}{2}}}{\Delta t} \\
\frac{\partial \mathbf{F}_n^x}{\partial c_{y_{n+1}}} = +f\left[\frac{\left(c_{y_{n+1}} - c_{y_{n-1}}\right)^2}{n_n^3} - \frac{1}{n_n}\right] \\
\frac{\partial \mathbf{F}_n^x}{\partial c_{y_{n-1}}} = +f\left[\frac{\left(c_{y_{n+1}} - c_{y_{n-1}}\right)^2}{n_n^3} + \frac{1}{n_n}\right] \\
\frac{\partial \mathbf{F}_n^y}{\partial c_{x_{n+1}}} = -f\left[\frac{\left(c_{x_{n+1}} - c_{x_{n-1}}\right)^2}{n_n^3} - \frac{1}{n_n}\right] \\
\frac{\partial \mathbf{F}_n^y}{\partial c_{x_{n-1}}} = -f\left[\frac{\left(c_{x_{n+1}} - c_{x_{n-1}}\right)^2}{n_n^3} + \frac{1}{n_n}\right]
\end{array}\right. \qquad (14)$$

where the discrete normalization factor n_n is given by:

$$n_n = \sqrt{\left(c_{x_{n+1}} - c_{x_{n-1}}\right)^2 + \left(c_{y_{n+1}} - c_{y_{n-1}}\right)^2}. \qquad (15)$$

This Jacobian is a sparse $2N \times 2N$ block tridiagonal matrix of bandwidth four. The iteration in Eq. 13 is calculated until convergence defined by $k < TOL$, where k is the norm of the sum of the forces $F_p + F_e$ and $TOL = 10^{-4}$.

3.2 Evolving Method

The previous method gives a direct link between the initial and final shape even if the final shape is far from the initial state. However the convergence can be very slow and the iterations oscillate as the constraint of being equal to $\mathbf{0}$ is too strong. In order to obtain a more robust method which follows closer to the physics, the dynamic Newton's law can be used. This method was used as well for solving the deformation of the material in [8]. The principle is to evolve the curve by making the force act on the acceleration of the evolution of the curve where an integration process gives a new curve evolving in time t. This method was also used to solve for the deformation in [11] for cloth and in [10] for muscle.

3.2.1 Set-up of the equation

Let the curve $\mathbf{c}$ be parameterized in space by s and evolve with the time parameter t, then the equation of motion is:

$$\frac{\partial}{\partial t}\left(\mathrm{d}m\,\frac{\partial \mathbf{c}}{\partial t}\right)(s,t) = \sum_i F_i(\mathbf{c}, s, t) \ , \qquad (16)$$

where $\mathrm{d}m$ is the mass of a small portion of the curve. This density is supposed to be constant for each position and at any time. It can arbitrarily be taken equal to one, for which the equation simplifies to:

$$\frac{\partial^2 \mathbf{c}}{\partial t^2}(s,t) = \mathbf{F}_p\left(\mathbf{c}, s, t\right) + \mathbf{F}_e\left(\mathbf{c}, s, t\right) + \mathbf{F}_d\left(\mathbf{c}_{,t}, s, t\right) \ , \qquad (17)$$

where $\mathbf{c}_{,s} = \frac{\partial \mathbf{c}}{\partial t}$. This is now a system of non-linear PDEs of the second order. In this case, the curve evolves along time and the complete Eq. 4 has to be taken into account. Moreover, the damping term has to be included to model the decrease in energy of the strings in order to obtain a steady state. Using simplified notation with $\frac{\partial u}{\partial x} = u_{,x}$, the complete system is written as:

$$\left\{\begin{array}{rl}
c_{x,tt} & = -\dfrac{F^\alpha}{2\pi}\,\dfrac{1}{\int_s c_y \sqrt{c_{x,s}^2 + c_{y,s}^2}\,\mathrm{d}s}\,\dfrac{c_{y,s}}{\sqrt{c_{x,s}^2 + c_{y,s}^2}} \\
& \quad + \left(\lambda\left(c_x - c_x^0\right)_{,s}\right)_{,s} - \mu\, c_{x,t} \\
c_{y,tt} & = \dfrac{F^\alpha}{2\pi}\,\dfrac{1}{\int_s c_y \sqrt{c_{x,s}^2 + c_{y,s}^2}\,\mathrm{d}s}\,\dfrac{c_{x,s}}{\sqrt{c_{x,s}^2 + c_{y,s}^2}} \\
& \quad + \left(\lambda\left(c_y - c_y^0\right)_{,s}\right)_{,s} - \mu\, c_{y,t}
\end{array}\right. \qquad (18)$$

The order of the system in time can be decreased by using the matrix form with the vector $\mathbf{U} = (\mathbf{c}, \mathbf{c}_{,t})$. In this case, Eq. 17 can be written as:

$$\begin{pmatrix} \mathbf{c} \\ \mathbf{c}_{,t} \end{pmatrix}_{,t} = \begin{pmatrix} 0 & 1 \\ 0 & 0 \end{pmatrix}\begin{pmatrix} \mathbf{c} \\ \mathbf{c}_{,t} \end{pmatrix} + \begin{pmatrix} 0 \\ \sum_i \mathbf{F}_i \end{pmatrix}. \qquad (19)$$

Denoting $M_{\mathrm{sys}} = \begin{pmatrix} 0 & 1 \\ 0 & 0 \end{pmatrix}$ and $\mathcal{F} = \begin{pmatrix} 0 \\ \sum_i \mathbf{F}_i \end{pmatrix}$, the matrix equation can be written as:

$$\mathbf{U}_{,t} = M_{\text{sys}} \cdot \mathbf{U} + \mathcal{F}.$$

3.2.2 Discretization with finite difference

In order to form a solution for the spatial derivative, finite differences are used (method of lines) [12]. The curve $\mathbf{c}$ is discretized by N positions separated by Δs (see Fig. 5).

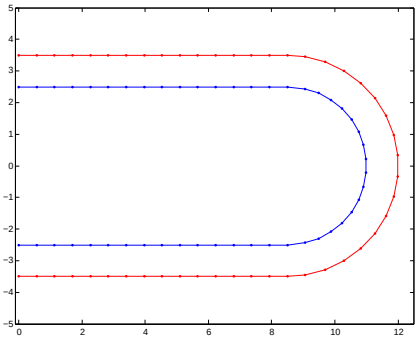

Fig. 5: Discretization of the initial position

Using the operator δ^1 for the central derivative (accuracy of second order),

$$\delta^1 \mathbf{c}(s) = \frac{\mathbf{c}(s+\Delta s) - \mathbf{c}(s-\Delta s)}{2\Delta s} \simeq \mathbf{c}_{,s}(s),$$

and the second order operator δ^2 for the second derivative such that:

$$\delta^2 \mathbf{c}(s) = \frac{\mathbf{c}(s+\Delta s) - 2\,\mathbf{c}(s) + \mathbf{c}(s-\Delta s)}{2\Delta s} \simeq \mathbf{c}_{,ss}(s)\ ,$$

the forces in Eq. 17 with a constant spring stiffness can then be written in the discrete form:

$$\begin{cases} \mathbf{F}_p = \frac{F^\alpha}{2\pi\, S^0} \frac{1}{\int_s c_y \sqrt{(\delta^1 c_x)^2 + (\delta^1 c_y)^2}\,\mathrm{d}s} \frac{\begin{pmatrix} -\delta^1 c_y \\ \delta^1 c_x \end{pmatrix}}{\sqrt{(\delta^1 c_x)^2 + (\delta^1 c_y)^2}} \\ \mathbf{F}_e = \lambda\, \delta^2 \left(\mathbf{c} - \mathbf{c}^0\right) \\ \mathbf{F}_d = -\mu\, \mathbf{c}_{,\mathbf{t}}, \end{cases}$$

where $\mathbf{F}_p$, $\mathbf{F}_e$ and $\mathbf{F}_d$ are three vectors of N components each, and Eq. 19 can be transformed into an ODE in time:

$$\mathbf{U}_{,t} = M_{\text{sys}}\, U + \underbrace{\begin{pmatrix} 0 \\ \mathbf{F}_p + \mathbf{F}_e + \mathbf{F}_d \end{pmatrix}}_{\mathcal{F}}, \qquad (20)$$

where $\mathbf{U}$ and $\mathcal{F}$ are now large vectors of $2N$ components and M_{sys} is a $2N \times 2N$ block matrix filled with zeros and the identity bloc.

3.2.3 Method of solution

A basic approach for solving the system of ODEs would be to use the forward Euler method in time using the relationship:

$$U(t+\Delta t) = U(t) + \Delta t \left(M_{\text{sys}}\, U(t) + \mathcal{F}(s)\right), \quad (21)$$

where Δt is the size of the time step of the discretization. This method is easy to implement, however this is a numerically explicit method and in order to have a stable solution, the time step Δt has to be taken small enough [11], and thus makes the calculation long. This phenomena appears especially if the coefficient λ is large, making the problem stiff [13]. Moreover, it is well known that an explicit method such as the Forward Euler Method makes the solution diverge. It is then hard to keep the strings oscillating in a bounded domain as they gain energy at each iteration. Therefore, an implicit method needs to be used [8, 14].

In the implicit approach, Eq. 21 is modified to obtain:

$$\mathbf{U}(t+\Delta t) = \mathbf{U}(t) + \Delta t \left(M_{\text{sys}}\, \mathbf{U}(t+\Delta t) + \mathcal{F}(t+\Delta t)\right). \qquad (22)$$

In this case, the time step can be taken arbitrarily large as the system becomes unconditionally stable (the only limitation is the accuracy of the result). However, solving Eq. 22 is much more complex, especially if the forces are non-linear. It is only advantageous to use the implicit method if terms make the system unstable.

The term $M_{\text{sys}}\, \mathbf{U}(t+\Delta t)$ is the integration term for the speed. It is a linear term and can directly go on the left hand side of the equation.

$$\left(\mathrm{I} - \Delta t\, M_{\text{sys}}\right)\mathbf{U}(t+\Delta t) = \mathbf{U}(t) + \Delta t\, \mathcal{F}(t+\Delta t). \quad (23)$$

This linear system must now be solved at each step. The force $\mathcal{F}$ has to be decomposed in order to be calculated implicitly.

The term $\mathbf{F}_e$ is the elastic term. It oscillates and needs to be made stable. The force is linear and can be expressed easily in matrix form:

$$\begin{pmatrix} 0 \\ \mathbf{F}_e \end{pmatrix} = \begin{pmatrix} 0 & 0 \\ \lambda\delta^2 & 0 \end{pmatrix} \mathbf{U} - \lambda\, \delta^2 \begin{pmatrix} 0 \\ \mathbf{c}^0 \end{pmatrix} = M_e\, \mathbf{U} - \mathbf{F}_d^0 \qquad (24)$$

It is well known from the spring-mass model used in cloth modeling that a better behavior (less deformable) is obtained by using more neighbors than

the two closest ones. Therefore, the elastic force was implemented by taking into account the first four neighbors at each position. The last two are given a smaller stiffness coefficient λ_2.

The term $\mathbf{F}_p$ is more complex in the sense that it is non-linear. This term cannot be solved directly by taking the inverse function. As it is linked to the derivative of the curve, this term also plays a role in the stiffness of the equation. In order to get a more stable behavior, a correction factor can be calculated by linearizing this force (see [15]). The function $\mathbf{F}_p$ depends on the vector $\mathbf{c}$. Therefore, approximating by a Taylor expansion, we have

$$\mathbf{F}_p\Big(\mathbf{c}(t+\Delta t)\Big) \simeq \mathbf{F}_p\left(\mathbf{c}(t) + \Delta t\,\frac{\partial \mathbf{c}}{\partial t}(t+\Delta t)\right) .$$

Next expanding the right hand side in a Taylor series gives the following expression:

$$\begin{aligned}\mathbf{F}_p\Big(\mathbf{c}(t+\Delta t)\Big) \simeq \quad & \mathbf{F}_p\Big(\mathbf{c}(t)\Big) \\ & + \sum_j \Delta t \frac{\partial \mathbf{c}^j}{\partial t}(t+\Delta t)\,\frac{\partial \mathbf{F}_p}{\partial \mathbf{c}^j}\Big(\mathbf{c}(t)\Big)\end{aligned}$$

Using the fact that $\mathbf{c}_{,t}$ is a variable of the system, the linearization is given in the following expression:

$$\mathbf{F}_p(t+\Delta t) = \mathbf{F}_p(t) + \Delta t \sum_j \frac{\partial \mathbf{F}_p}{\partial \mathbf{c}^j}\,\mathbf{c}^j_{,t}(t+\Delta t). \quad (25)$$

Let us denote the Jacobian matrix as $\frac{\partial \mathbf{F}_p}{\partial \mathbf{c}}$ such that:

$$\left(\frac{\partial \mathbf{F}_p}{\partial \mathbf{c}}\right)_{i,j} = \frac{\partial \mathbf{F}^i_p}{\partial \mathbf{c}^j} .$$

Eq. 25 is linear in $\mathbf{c}$ and can be written in the matrix form:

$$\begin{pmatrix} 0 \\ \mathbf{F}_p(t+\Delta t) \end{pmatrix} = \begin{pmatrix} 0 \\ \mathbf{F}_p(t) \end{pmatrix} + \Delta t \begin{pmatrix} 0 & 0 \\ 0 & \dfrac{\partial \mathbf{F}}{\partial \mathbf{c}} \end{pmatrix} \mathbf{U}. \quad (26)$$

The matrix $\Delta t \begin{pmatrix} 0 & 0 \\ 0 & \frac{\partial \mathbf{F}}{\partial \mathbf{c}} \end{pmatrix}$ is denoted as dM_p. This term will correct the instability during the iteration by adding it on the left hand side of Eq. 23.

The damping term is linear and can be placed on the other side as well, however this term is already a stabilization term. It makes very little difference whether it is used as an implicit one or not. This force can also be expressed in matrix form:

$$\begin{pmatrix} 0 \\ \mathbf{F}_d \end{pmatrix} = -\mu \begin{pmatrix} 0 & 0 \\ 0 & \mathrm{I} \end{pmatrix} \mathbf{U} = M_d\,\mathbf{U}. \quad (27)$$

Now Eq. 24, 26 and 27 are substituted into Eq. 23 to give:

$$\begin{aligned}&\Big[\mathrm{I} - \Delta t\Big(M_{\mathrm{sys}} - M_e - \Delta t\, dM_p\Big)\Big]\,\mathbf{U}(t+\Delta t) = \\ &\Big(\mathrm{I} + \Delta t\, M_d\Big)\,\mathbf{U}(t) + \begin{pmatrix} 0 \\ \mathbf{F}_p(t) \end{pmatrix} - \begin{pmatrix} 0 \\ \mathbf{F}^0_d \end{pmatrix} ,\end{aligned} \quad (28)$$

or in matrix block form:

$$\begin{pmatrix} \mathrm{I} & -\Delta t\,\mathrm{I} \\ -\Delta t\,\lambda\,\delta^2 & \mathrm{I} - (\Delta t)^2\,\dfrac{\partial \mathbf{F}_p}{\partial \mathbf{c}} \end{pmatrix} \begin{pmatrix} \mathbf{c} \\ \mathbf{c_t} \end{pmatrix}(t+\Delta t) =$$

$$\begin{pmatrix} \mathrm{I} & 0 \\ 0 & (1-\mu)\,\mathrm{I} \end{pmatrix} \begin{pmatrix} \mathbf{c} \\ \mathbf{c_t} \end{pmatrix}(t) + \begin{pmatrix} 0 \\ \mathbf{F_p} \end{pmatrix}(t) - \begin{pmatrix} 0 \\ \mathbf{F}^0_d \end{pmatrix}. \quad (29)$$

This equation is solved for at each iteration and the stopping condition is reached when the sum of forces $\|\mathbf{F}_e + \mathbf{F}_e\| < \epsilon$ with $\epsilon \simeq 10^{-4}$. The Jacobian is calculated numerically by finite differences. Some trade-off between convergence and calculation speed is done by recalculating this matrix only at some iterations (typically every ten iterations).

3.3 Numercial Calculation of the Length, Area and Volume

The shape is discretized for the desired resolution, then characteristics such as length, area and filled volume have to be calculated based on the discrete case. The shape is assumed to be piecewise linear between the discrete positions. Exact formulas can then be taken to calculate these characteristics with this hypothesis. The approximation of the real volume therefore has an accuracy of second order. Let us call $\mathbf{c}^k$ the k^{th} component of $\mathbf{c}$.

3.3.1 Length

The length of the curve is calculated by summing the length of all the linear sections:

$$\mathcal{L} = \sum_{i=0}^{i=N-2} \sqrt{\Big(c_x^{i+1} - c_x^i\Big)^2 + \Big(c_y^{i+1} - c_y^i\Big)^2}. \quad (30)$$

3.3.2 Area

The area under the 2 dimensional curve is calculated by summing each trapezoid between each discrete position (see Fig. 6):

$$\mathcal{A} = \frac{1}{2} \sum_{i=0}^{i=N-2} \Big|\big(c_x^{i+1} - c_x^i\big)\,\big(c_y^{i+1} + c_y^i\big)\Big| . \quad (31)$$

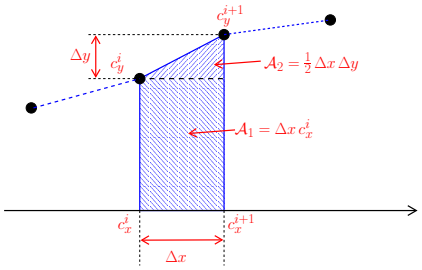

Fig. 6: Calculation of the area under the curve

3.3.3 Volume

The volume filled by the balloon is calculated by summing the portion of cones along the axis of rotation. (see Fig. 7) Each cone has a volume:

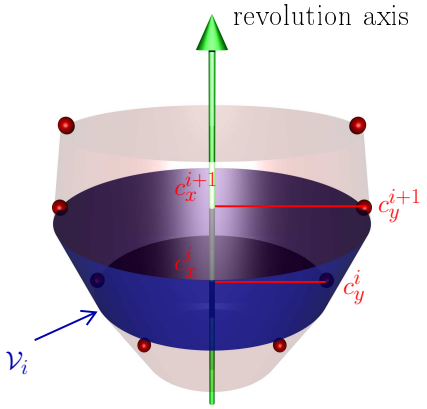

Fig. 7: A cone used to approximate a portion of the balloon in three dimensions

$$\mathcal{V}_i = \int_{c_x^i}^{c_x^{i+1}} \pi\, c_y^2(s)\,\mathrm{d}s \tag{32}$$

with

$$c_y(s) = c_y^i \left(\frac{c_x^{i+1} - s}{c_x^{i+1} - c_x^i}\right) + c_y^{i+1} \left(\frac{s - c_x^i}{c_x^{i+1} - c_x^i}\right),$$

Changing variables, Eq. 32 can be rewritten as:

$$\mathcal{V}_i = \pi \left(c_x^{i+1} - c_x^i\right) \int_0^1 \left(c_y^{i+1}\, s + c_y^i\,(1-s)\right)^2 \mathrm{d}s.$$

With a second change of variables, $Z = c_y^{i+1}\, s + c_y^i\,(1-s)$:

$$\begin{cases} \mathcal{V}_i = \pi \left(c_x^{i+1} - c_x^i\right) \dfrac{1}{c_y^{i+1} - c_y^i} \displaystyle\int_{c_y^i}^{c_y^{i+1}} Z^2\,\mathrm{d}Z \\ \qquad \text{if } c_y^{i+1} \neq c_y^i \\ \\ \mathcal{V}_i = \pi \left(c_x^{i+1} - c_x^i\right) \displaystyle\int_0^1 \left(c_y^i\right)^2 \mathrm{d}s \\ \qquad \text{if } c_y^{i+1} = c_y^i \end{cases}$$

$$\Rightarrow \mathcal{V}_i = \frac{\pi}{3} \left(c_x^{i+1} - c_x^i\right) \left[\left(c_y^{i+1}\right)^2 + c_y^{i+1}\, c_y^i + \left(c_y^i\right)^2\right]. \tag{33}$$

Therefore the volume of the balloon is known from points only in the right hand side of the cone (where $c_y^i > 0$):

$$V = \frac{\pi}{3} \sum_{i=0}^{i<\frac{N}{2}} \left(c_x^{i+1} - c_x^i\right) \left[\left(c_y^{i+1}\right)^2 + c_y^{i+1}\, c_y^i + \left(c_y^i\right)^2\right]. \tag{34}$$

4 Results

4.1 Direct Method

With the direct solution using Newton's method of finding the roots, the balloons converge to a shape which is effectively different from a sphere (see Fig. 8).

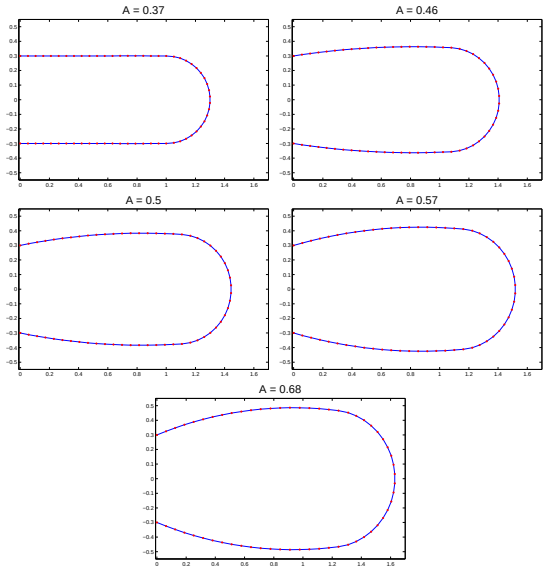

Fig. 8: Shape obtained with the direct method for different pressures. The parameter A corresponds to the normalized area filled by the interior curve.

However, the iterations oscillate with overshoots during the solving process and converge slowly when the

pressure becomes too large. In order to obtain faster convergence, the second method is used.

4.2 Evolving Method

This method gives a convergence without oscillations, and the stability is far better. The balloons can be dilated without slowing down the convergence. The evolution of the force due to pressure and the membrane action at each position is shown for some iterations between the initial and final states in Fig 9.

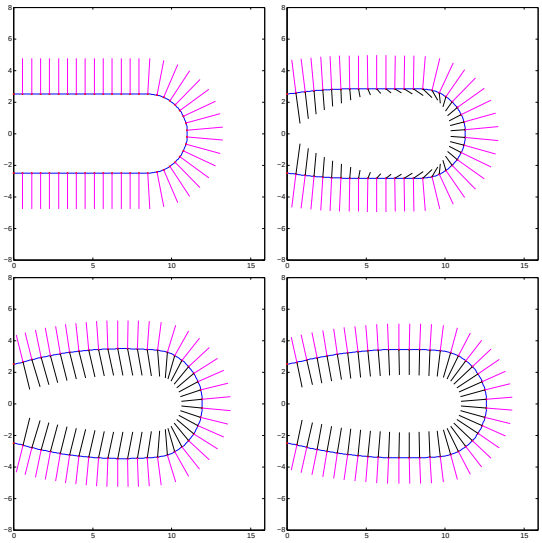

Fig. 9: Evolution of the convergence of a balloon for a fixed pressure. The red points are the discrete positions, the magenta lines shows the elastic forces acting on the membrane and the black vectors are the forces of pressure acting at each position. When the equilibrium is reached, pressure and elastic forces compensate each other.

The evolution of the norm $\|\mathbf{F}_p + \mathbf{F}_e\|$ during the iterations is shown in Fig. 10. Notice that the value of this sum is always decreasing with each iteration which makes the method very stable, and the convergence is linear close to the solution of the static state.

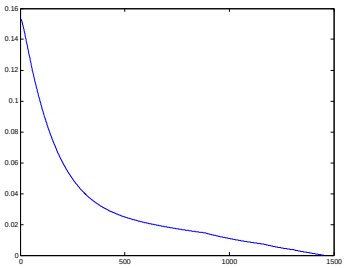

Fig. 10: Plot of the norm of the sum of elastic and pressure forces for each iteration illustrating convergence of the method

Figure 11 shows the deformation between the two membranes. The deformation of the midwall can be seen. Except for some elongation, the base doesn't have significant deformation due to the fixed positions. However, a change in the wall thickness can be seen at the apex by a contraction of the mesh. The three dimensional volume can be reconstructed

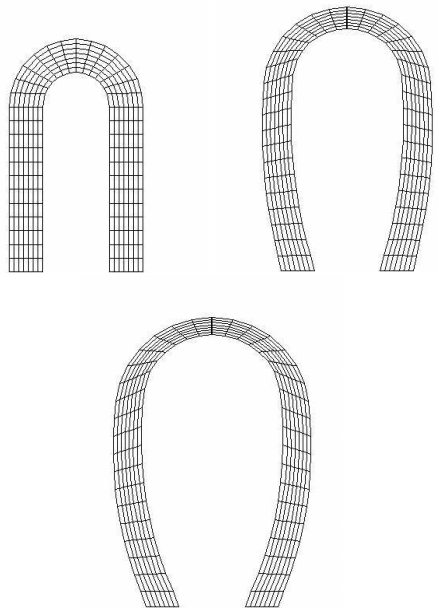

Fig. 11: Deformation of the two membranes and mesh interposed between them. Three increasing pressures are applied to the inter membrane. The mesh is interpolated between the two membranes.

by revolution. A realistic shape of a dilated and contracted balloons can be seen in Fig. 12.

Physically, the spaces separating the two balloons are filled with water. The hypothesis of the incompressibility of water should then result to a constant volume (or area in $2D$) between the two membranes. In the simulation, even with large deformations, the difference in area between rest and dilated position is less than a percent (due to the discretization and numerical errors).

5 Tomography

5.1 Methods

5.1.1 Filling and orientation of the balloon

In order to evaluate a tomographic experiment using the Jaszczak Dynamic Phantom a simulation of the two balloons with realistic motion was performed. To

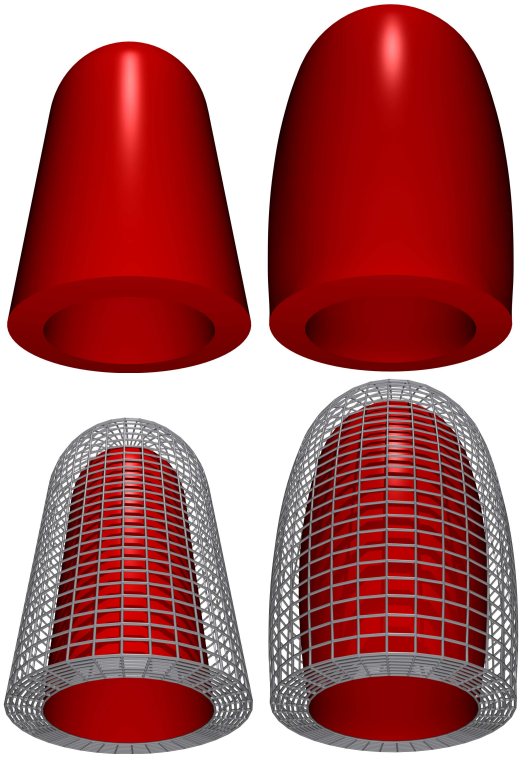

Fig. 12: Deformation of the balloons in 3D. Pictures at the top are volumetric visualizations and the pictures on the bottom show a mesh for the outer simulated wall of the heart. For top and for bottom the visualization shows the rest state (left) and the final state (right) for an interior volume increased by sixty percent.

be consistent with the realized study, the initial state was a cylindrical shape. The balloons were then dilated to reach an ejection fraction of 60% calculated as

$$\frac{\mathcal{V}_{dilate} - \mathcal{V}_{rest}}{\mathcal{V}_{rest}} = 0.6 \ . \tag{35}$$

The balloon was also rotated into a position that simulated the orientation of the heart in the body when the camera is rotating around it. An angle of rotation of 45° was chosen around the two axes $\mathbf{e}_x$ and $\mathbf{e}_y$ (where $\mathbf{e}_y$ is the long axis of the body) in Fig. 13.

5.1.2 Camera and timing settings

The simulation was set-up so that the camera rotated around the z axis in Fig. 13. Parallel ray projections were formed over the entire volume of the heart. It was assumed that the heart beat at a rate of 65 beats per minute. The camera rotated around 180° and 90 angular samples were taken.

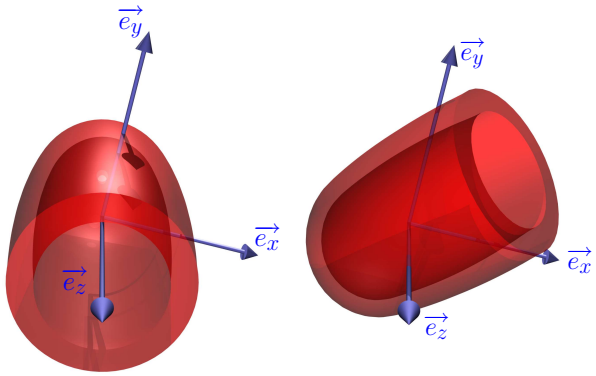

Fig. 13: The picture on the left shows the initial orientation without rotation, the picture on the right shows the orientation of the heart as in the body with $\mathbf{e}_y$ aligned with the long axis of the body.

5.1.3 Projection and reconstruction settings

For each angle, a projection image was calculated. Figure 14 shows an example of projection images at three angular positions.

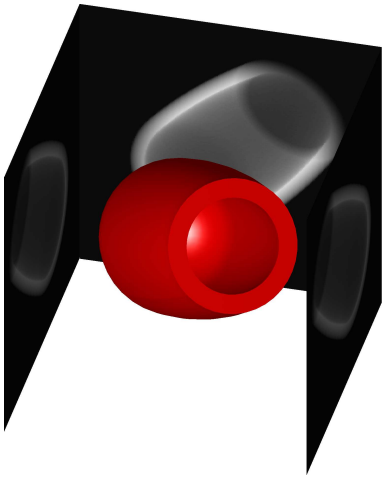

Fig. 14: Example of projections for three angles around the balloon. The balloon is inclinated at 45° and is static in this case.

In the dynamic case, each projection at a particular angle depended upon the heart position in the cardiac cycle. Thus for a particular time (angle), the corresponding position of the heart was calculated and then the corresponding volume was projected. The projected data consisted of 90 projections which were not consistent due to the motion. Each reconstructed intensity distribution was voxelized in a volume of 256^3 voxels. The reconstruction of the volume was performed by filtered-back projection, slice by slice.

5.2 Results

A simulation of a static case (no beating heart) was first performed. For this example the reconstruction gave exactly the original shape of the balloon as seen in Fig. 15.

Figure 16 shows the results for the first dynamic experiment where the data were assumed to be acquired during a very short period of time like a dynamic CT measurement. For each angle, virtually an instantaneous projection was performed by rotating the camera at 2° per second. It was assumed that this short acquisition was not subject to noise, so only the artifacts due to the motion could be visible (and the artifacts due to the sampling of the angle).

The angle to angle inconsistency of the projected data creates artifacts which lead to a non-uniformity for the reconstruction of the tracer intensity on the wall and a non-null intensity outside of the boundaries of the wall. The exact non-uniformity depends on the position of the heart for each angle and also depends on the frequency of the beating. The results of the reconstruction are shown in Fig. 16 for a normal heart beating at 65 beats per minutes.

Figure 17 shows results of the simulation of a long acquisition time much like that performed in a PET or SPECT study. In this case, for each angle, the camera was stationary during enough time to record at least a full cardiac cycle. The projections were then the average of the complete motion. Thus for each angle the projections were summed over time. In this case, the artifacts caused by the motion are a blurring in the direction of the displacement. The apex of the balloon which has a displacement along the axis of the cylinder shows a large blurring effect along that axis. The wall of the balloon is essentially displaced in the perpendicular direction.

6 Conclusion and Future Work

Physical forces were taken into account to set-up equations of equilibrium and equations of motion for an elastic membrane filled with water which exerted an internal pressure on the elastic membrane. Two methods were used to solve the physical problem. One method involved obtaining a direct solution of the equations of equilibrium (static method) whereas the second method involved a method of evolution were the force of acceleration acts upon the system as it evolves over time (dynamic method). The two approaches provide two different systems of non-linear equations which were both solved numerically using finite difference methods. The results for both converge to similar non-trival[2] shapes.

The two finite difference methods are differentiated by their speed of convergence. For a very small change of internal pressure, the first method converges quickly to the final solution since the shape is initially very close to the final one. However, for a larger pressure force, oscillations and overshoots are visible during the iteration process. The stability of the method due to numerical errors then becomes a problem. Moreover, the water filled region between the two membranes should be constant due to conservation of volume. However, since the simplified Eq. 3 is used, it is not obvious how to scale the factor f in order to insure that the area of this region is constant. This factor indeed depends on the volume of the balloon and then on the final position of $\mathbf{c}$. So f has to be chosen differently for the exterior membrane than for the interior membrane. But this relationship is not known a priori since the final shape has not been determined. Therefore to obtain this condition f has to be determined by trial and error.

For these reasons, the second method is preferred, especially when the deformation becomes large. The shape does not oscillate during convergence and the norm of the sum of the forces is always decreasing indicating good stability. In this case, the complete equation is taken so the link between the two membranes is then automatically taken into account. An implicit method is used to solve the system of discretized ODEs for each step.

It can be noticed that the string term $\mathbf{F}_e$ of Eq. 6 is intended to create an oscillation with a constant energy in time. However, since the first order implicit Euler's method is used, it is well known that the solution will decrease to zero if the time step is too large. This phenomena can be avoided by using the trapezoidal rule and mixing half implicit with half explicit numerical methods [12, 13]. However, the decreasing phenomenon is not a problem since this is the desired behavior. Moreover, this numerical decrease is small compared to the decrease effect caused by the addition of a damping force.

The system of PDEs of the second method is more complex than for the first method, and in that case, the Jacobian of the pressure force is only calculated approximately and is not updated at each iteration. However, the dynamic method evolves the curve smoothly between the initial and the final position, so the exact value is not necessary for convergence.

The methods presented for solving for the shapes of the balloons can be used to simulate a beating heart in a tomographic simulation. Two dynamic experiments were tested: one with a short and one with a

[2] in the sense that the final form is not circular

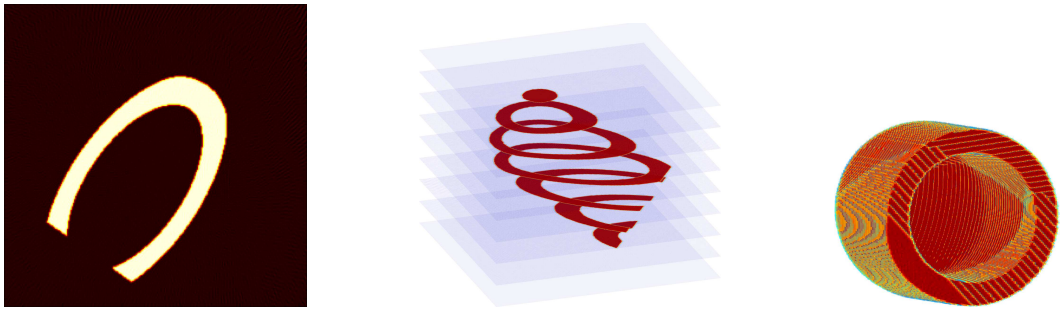

(a) (b) (c)

Fig. 15: Reconstruction for the static case. Figure (a) shows a single slice of the reconstruction following the correct boundaries of the balloon with zero intensity outside. Figure (b) shows some slices of the balloon. Figure (c) is the visualization of a large number of slice showing the reconstructed shape of the balloon in space.

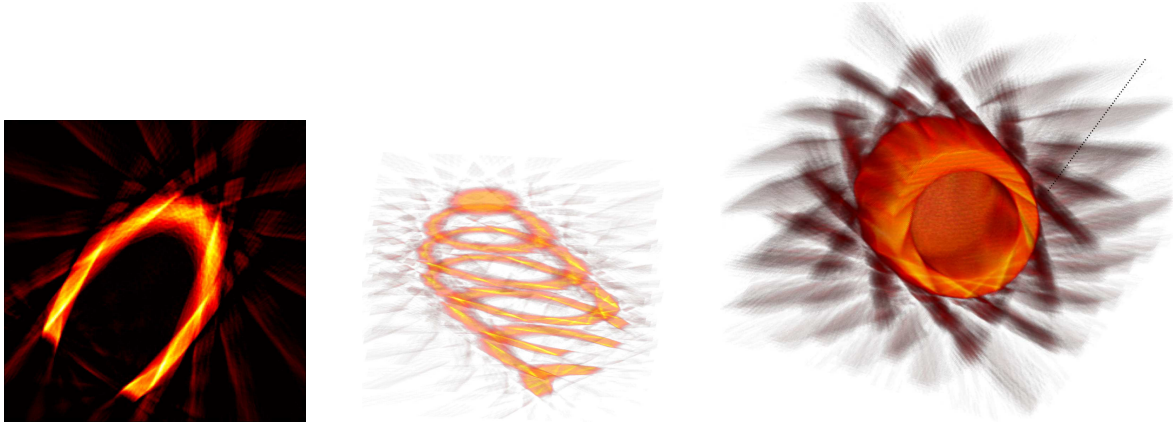

(a) (b) (c)

Fig. 16: Reconstruction of the short sampling for the dynamic acquisition. Figure (a) shows a single slice of the reconstruction, the non-uniformity in the heart wall is visible. Figure (b) shows some slices of the wall. The boundary is oscillatory and some artifacts propagate outside the wall. Figure (c) is a reconstruction of a large number of slices, the dissipation of the artifacts outside of the wall can be noticed.

longer acquisition time. In the simulations the following approximations were assumed:

1. The dynamics of the balloon modeled motion of the left ventricle.
2. The projections were free of attenuation.
3. The projections were free of noise.
4. The camera rotated around the heart, simulated by the balloon, in a perfect circle.
5. The projections were performed on a voxelized volume where each voxel was assumed to have the same concentration of tracer, despite the fact that there was contraction and dilation of the volume.

The first assumption indeed results in a large approximation. The balloon is an extremely simplified model for the left ventricle. The base is not moving and no twisting motion due to the presence of muscle fibers is taken into account [16, 17]. A 2-dimensional curve, such as used in this study, cannot model this complex motion. However, this experiment gives a rough approximation to the motion of the boundaries of the heart wall, especially for a low quality acqui-

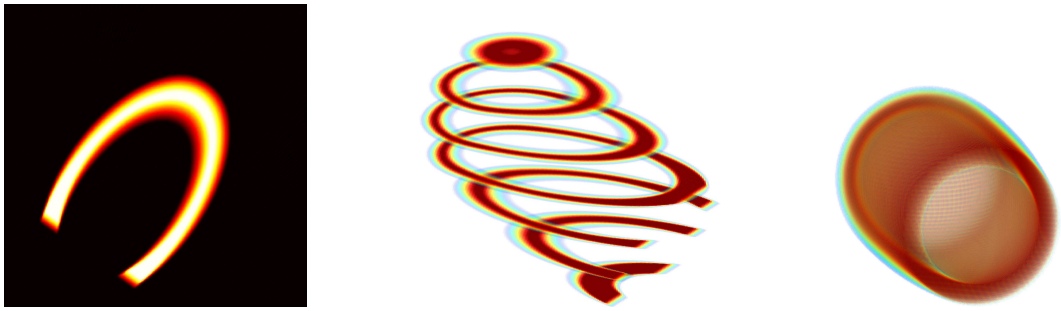

(a) (b) (c)

Fig. 17: Reconstruction of the long sampling for the dynamic acquisition. Figure (a) shows a single slice of the reconstruction, the blurring surrounding the heart wall is visible. Figure (b) shows some 3D slices of the heart. The artifacts don't propagate outside of the wall. Figure (c) is a reconstruction of a large number of slices, the global form of the balloon is conserved but the motion blurs the boundaries.

sition such as SPECT. The results help to give an idea of some of the artifacts due to the heart beating. It also can be used to compare with imaging experiments using the Jaszczak Dynamic Cardiac Phantom.

The following two assumptions are also large approximations. It is hard to compare this model with a real SPECT experiment but may be more representative of an x-ray CT acquisition. Especially in the short time acquisition, the noise of the data is very large due to the lack of counts. However, the model was performed to simulate the motion, so that attention is given only to the motion distortion without taking in account other kinds of artifacts such as those due to noise.

The fourth point would have to be taken into account for a true SPECT simulation where attenuation results in inconsistencies in the data. The backprojection of rays will propagate artifacts in a direction which depends on the position of the balloon.

The last assumption does not produce large errors in the study. The variation of tracer concentration per voxel is actually very small, especially since a large volume is used (256^3 voxels).

The results of this study show that the long acquisition time actually gives a better approximation of the motion than a fast dynamic acquisition due to the averaging of the projections. There is less propagation of the artifacts into the background.

Future work includes the validation of the numerical solutions by comparing the results with a CT and a SPECT scan of the real beating balloon in the Jaszczak Dynamic Cardiac Phantom. A study in real $3D$ of the motion could be performed. In this case, the twisting movement of the heart could be studied by adding constraints on the shape.

Appendix: Particular Analytical Solution to the Differential Equation

We show in this appendix that the term z^0 of the initial shape in Eq. 11 is actually responsible for making the equation non-linear. The equation is then considered with a rest state for the spring at ${z^0}'' = 0$. This means that the springs are initially contracted in a single line between the two fixed positions (in three dimension, the initial shape is therefore a disc). Then the new equation is

$$z'' + i\,\frac{f}{\lambda}\,\frac{z'}{|z'|} = 0\ .$$

It is first shown than the non-linear term $|z'|$ is actually constant. This can be easily shown in the complex case by expressing the derivative of the squared modulus of a complex function:

$$\left(|z|^2\right)' = 2\mathbb{R}_e(\overline{z}\,z').$$

So taking the derivative:

$$\left(|z'|^2\right)' = 2\mathbb{R}_e(\overline{z'}\,z'')\ ,$$

and using the equation:

$$\left(|z'|^2\right)' = -2\frac{f}{\lambda}\mathbb{R}_e(i\frac{\overline{z'}\,z'}{|z'|})$$

$$\Rightarrow \left(|z'|^2\right)' = -2\frac{f}{\lambda}\mathbb{R}_e(i|z'|) = 0.$$

Let us denote C the constant $|z'|$. The new equation is now linear

$$z'' + i\,\frac{f}{\lambda C}\,z' = 0\ .$$

This is now easily solved with the initial condition $z(0) = i\,R$ and $z(1) = -i\,R$. Setting $\mu = \frac{f}{\lambda C}$ we have:

$$z(s) = \frac{2i\,R}{1-e^{-i\mu}}\,e^{-i\,\mu s} - \frac{R\left(1-e^{-i\,\mu}\right)}{1-e^{-i\mu}}\ .$$

In real variable notion this reduces to:

$$\left\{\begin{array}{l} c_x(s) = \alpha\sin(\mu\,s-\varphi)+\beta \\ c_y(s) = \alpha\cos(\mu\,s-\varphi) \end{array}\right.\ , \tag{36}$$

where

$$\left\{\begin{array}{l} \alpha = \dfrac{2\,R}{\cos(\mu)-1}\sin\left(\dfrac{\mu}{2}\right) \\ \\ \beta = \dfrac{R}{\cos(\mu)-1}\sin(\mu) \\ \\ \varphi = \mathrm{Arctan}\left(\dfrac{\sin(\mu)}{\cos(\mu)-1}\right) \end{array}\right.$$

Finally, C can be expressed with the initial shape. $|z'|$ is constant so $|z'| = |z^{0'}|$ with $z^0 = (1-2\,s)\,iR$. Then $|z'| = C = 2R$. An example is shown in Fig. 18 where the initial position is a straight line.

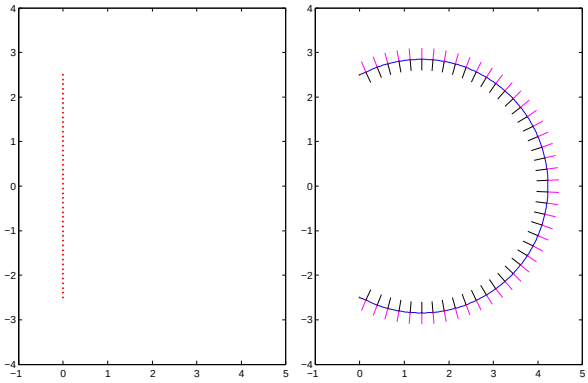

Fig. 18: Numerical validation of the circle solution for an initial position with vanishing second derivative. The picture on the left shows the initial position of the membrane making a straight line from the first to the last point. The picture on the right is the final shape after dilatation. This shape has converged to a portion of a circle.

Acknowledgement

The authors acknowledge Michlel Defrise for the comment on the equation. This work was supported by NIH Grant R01 EB000121 and U.S. Department of Energy (DOE) under contract DE-AC02-05CH11231.

References

[1] Eric Bardinet, Laurent D. Cohen, and Nicholas Ayache. Analyzing the deformation of the left ventricle of the heart with a parametric deformable model. Technical Report technical report : RR-2797, INRIA, February 1996.

[2] Burkhard Wunsche. The visualization and measurement of left ventricular deformation. In *Proceedings of the First Asia-Pacific bioinformatics conference on Bioinformatics*, pages 119–128. Australian Computer Society, Inc., 2003.

[3] Xenophon Papademetris and James S. Duncan. Cardiac image analysis: Motion and deformation. In J. M. Fitzpatrick and M. Sonka, editors, *Handbook on Medical Imaging - Volume III: Medical Image Processing and Analysis*. SPIE, 2000.

[4] Arkadiusz Sitek, Gregory J. Klein, Grant T. Gullberg, and Ronald H. Huesman. Deformable model of the heart with fiber structure. *IEEE, Transaction on Nuclear Science*, 49(3):789–93, June 2002.

[5] Alexander I. Veress, Grant T. Gullberg, and Jeffrey A. Weiss. Measurement of strain in the left ventricle during diastole with cine-MRI and deformable image registration. *Journal of Biomechanical Engineering*, 127(1):1195–207, December 2005.

[6] Alexander I. Veress, W. Paul Segars, Benjamin M.W. Tsui, and Grant T. Gullberg. Normal and pathological NCAT image and phatom data based on physiologically realistic left ventricle finite element models. *IEEE, Transaction on Medical Imaging*. In Press.

[7] Arkadiusz Sitek, Gregory J. Klein, Bryan W. Reutter, Ronald H. Huesman, and Grant T. Gullberg. Measurement of the biomechanics of 3-D cardiac function with gated nuclear medicine studies. *In: Conference Record of the 2005 IEEE Nuclear Science Symposium and Medical Imaging Conference*, 4:2346–49, October 2005.

[8] Demetri Terzopoulos, John Platt, Alan Barr, and Kurt Fleischer. Elastically deformable models. In *Proceedings of the 14th Annual Conference on Computer Graphics and Interactive Techniques*, pages 205–214, New York, NY, USA, 1987. ACM Press.

[9] Erwin Kreyszig. *Differential Geometry*. Dover Publications, 1991.

[10] L. P. Nedel and D. Thalmann. Real time muscle deformations using mass-spring systems. In *Proceedings of the Computer Graphics International*, page 156, Washington, DC, USA, 1998. IEEE Computer Society.

[11] Xavier Provot. Deformation constraints in a mass-spring model to describe rigid cloth behavior. In Wayne A. Davis and Przemyslaw Prusinkiewicz, editors, *Graphics Interface*, pages 147–154. Canadian Human-Computer Communications Society, 1995.

[12] K.W. Morton and D.F. Mayers. *Numerical Solution of Partial Differential Equations*. Cambridge, 2005.

[13] E. Haier, S. P. Norsett, and G. Wanner. *Solving Ordinary Differential Equations I, Nonstiff Problems*. Springer, 2000.

[14] David Baraff and Andrew Witkin. Large steps in cloth simulation. *Computer Graphics*, 32(Annual Conference Series):43–54, 1998.

[15] Young-Min Kang, Jeong-Hyeon Choi, Hwan-Gue Cho, and Chan-Jong Park. Fast and stable animation of cloth with an approximated implicit method. In *Computer Graphics International*, pages 247–256, 2000.

[16] Henry M. Spotnitz. Macro design, structure, and mechanics of the left ventricle. *The Journal of Thoracic and Cardiovascuar Surgery*, 119(5):1053–1077, May 2000.

[17] Arkadiusz Sitek, Gregory J. Klein, Grant T. Gullberg, and Ronald H. Huesmann. Deformable model of the heart with fiber structure. *IEEE, Transaction on Nuclear Medicine*, 42(3):789–793, June 2002.